Cheerambathur et al., http://www.jcb.org/cgi/content/full/jcb.200611113/DC1

Supplemental results

Experimental investigation of the molecular mechanism of the change in MT dynamics at anaphase B onset

To understand the molecular mechanism regulating the spatial change in MT dynamics and EB1 distribution, we inhibited several players thought to play an important role in anaphase B spindle elongation in *Drosophila* embryos.

KLP3A. One candidate protein is the kinesin KLP3A, previously shown to localize to the spindle midzone during anaphase B and to affect the flux to sliding switch at anaphase B onset (Brust-Mascher et al., 2004). KLP3A is required for the organization of ipMT bundles (Kwon et al., 2004) and might thus contribute to the spatial regulation of MT dynamics. We performed antibody inhi-

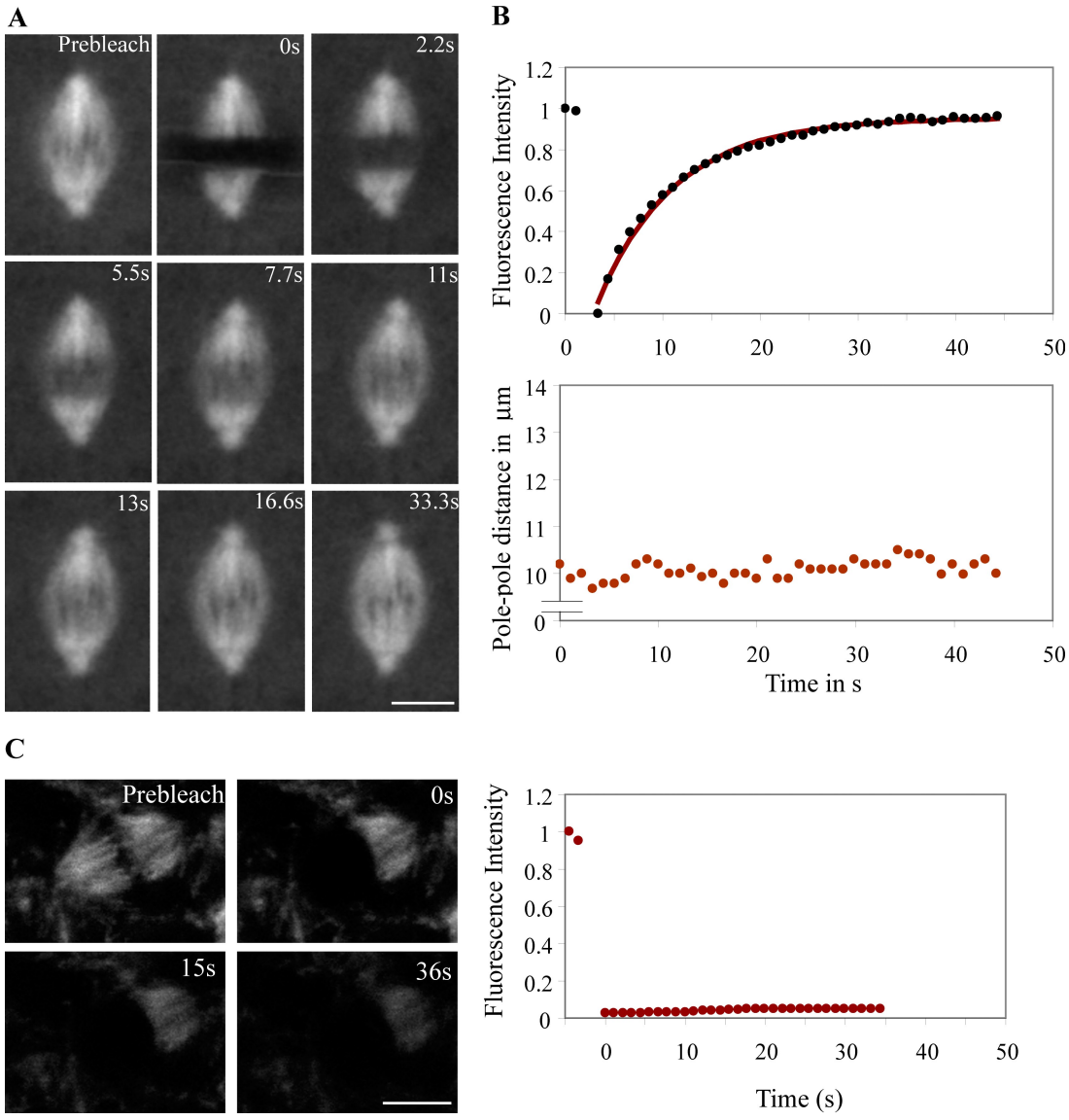

Figure S1. **MT dynamics in the *Drosophila* spindle by FRAP.** (A and B) Microtubules in *Drosophila* mitotic spindles turn over very rapidly with a half-time of 5–6 s. (A) Frames from a time-lapse video of a metaphase spindle in a GFP-tubulin–expressing *Drosophila* embryo photobleached in a 2.5-µm-wide region at the spindle equator. The spindle recovered its fluorescence in 30 s, and the recovery is uniform within the bleached zone. Bar, 5 µm. (B) The normalized mean fluorescence intensity of the bleached region (black dots) was plotted against time and the half-time ($t_{1/2}$ = 5.5 s) was obtained by fitting a single exponential curve (brown line) to the recovery. A constant spindle length of 10 µm indicates that the spindle is in pre-anaphase B (bottom). (C) Micrographs of a spindle bleached in an embryo injected with 1 mM taxol. Note that the spindle does not recover its fluorescence even after 36 s. The normalized fluorescence recovery plot is shown on the right. Bar, 5 µm.

bitions against KLP3A to see whether KLP3A's localization to the midzone might contribute to the observed spatial regulation of MT dynamics, as KLP3A affects ipMT bundling in anaphase B. We injected function blocking anti-KLP3A antibody (Brust-Mascher et al., 2004; Kwon et al., 2004) into the EB1-GFP–expressing embryos. However, in those spindles that were observed to be disorganized and performed slight anaphase B, there was an associated reorganization of EB1 (Fig. S2 D).

Ran gradient. The Ran pathway is thought to play an important role in establishing gradients associated with the mitotic spindle and is therefore a candidate for regulating the observed catastrophe gradient that we report. The injection of the Ran inhibitor RanT24N (obtained from A. Wilde, University of Toronto, Toronto, Canada), which is locked in the GDP-bound state (16 mg/ml), generates a plethora of defects, including no spindle assembly and the assembly of truncated spindles (Silverman-Gavrila and Wilde, 2006). In the assembled short spindles, we observed spindle elongation to 12–13 µm accompanied by an EB1-GFP redistribution at anaphase B onset (Fig S2 D). In addition, the FRAP recovery dynamics observed on these spindles was quite similar to wild type (unpublished data).

Mathematical estimates of MT lengths and turnover time

For a given choice of MT dynamic instability parameter rates, the growth and shortening rates, v_g and v_s, and the rescue and catastrophe frequencies, f_{res} and f_{cat}, the mean length of MTs that undergo dynamic instability is either a constant,

$$< L >= \frac{v_g v_s}{v_s f_{cat} - v_g f_{res}} \text{ (bounded regime),}$$

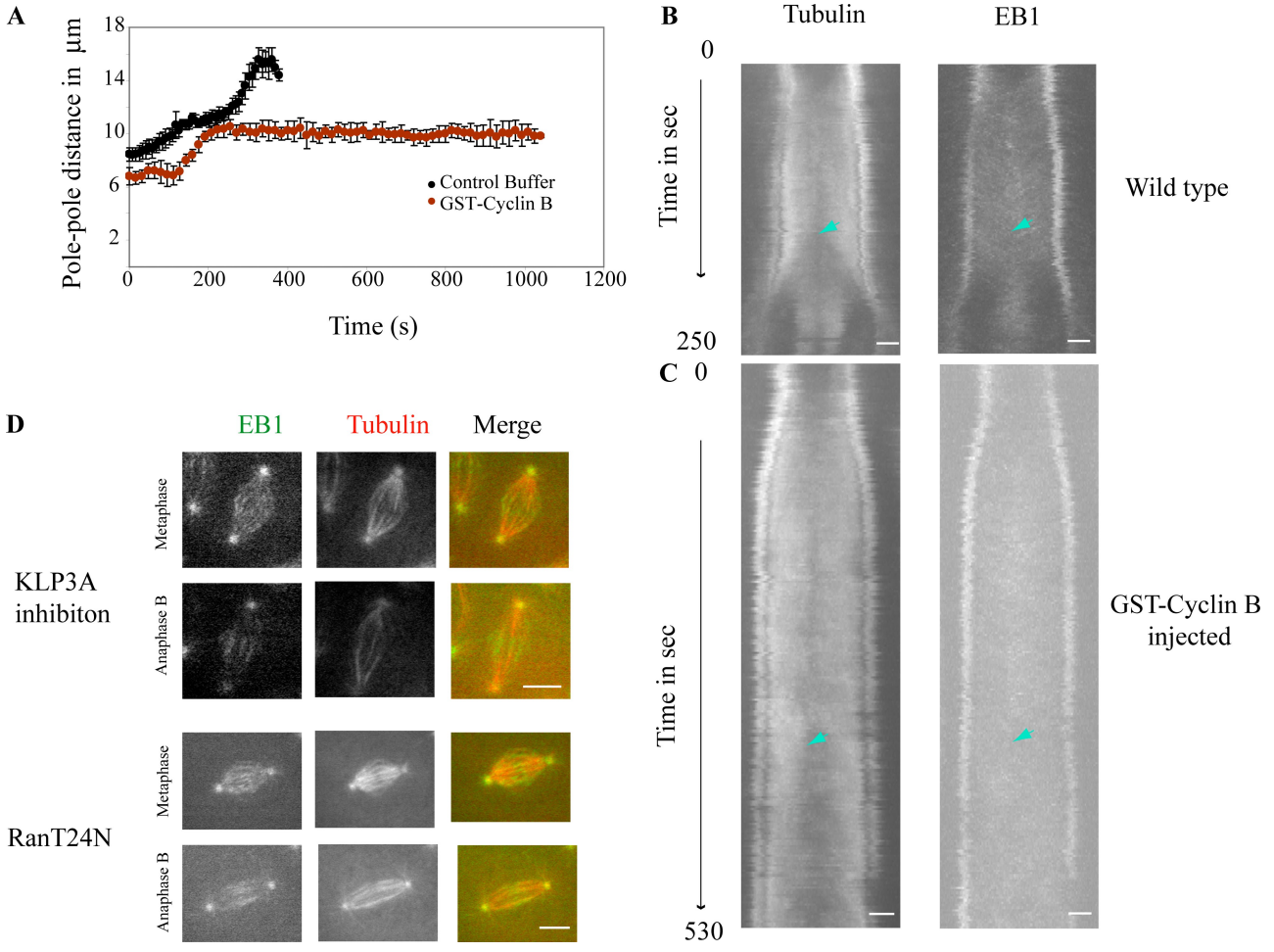

Figure S2. **Spindle dynamics in the presence of stable GST–cyclin B, anti-KLP3A, and RanT24N.** (A) Pole–pole distance of spindles in embryos injected with stable GST–cyclin B or buffer. Each plot shows the mean value of 15 spindles. (B and C) Total fluorescence intensity of tubulin and EB1 across a spindle over the entire mitosis in wild-type and cyclin B–injected embryos. (B) In the tubulin kymograph, anaphase A onset (blue arrowhead) is marked by a region of reduced intensity moving toward the pole. Note that in the corresponding EB1 kymograph on the right the EB1 fluorescence shows no change in distribution at this time. (C) In the presence of stable cyclin B, the EB1 fluorescence remains the same even long after anaphase A onset (see arrowhead in the kymographs). (D) Micrographs show EB1-GFP distribution in embryos injected with rhodamine tubulin and the inhibitors for KLP3A or Ran during metaphase and anaphase B. Note that in both cases, the spindle does elongate slightly during anaphase B and the EB1-GFP redistribution still occurs. Bars, 5 µm.

or increasing with time <*L(t)*> (unbounded regime), depending on whether the sign of the expression ($v_s f_{cat} - v_g f_{res}$) is positive or negative, respectively (Verde et al., 1992). The characteristic lengths by which the MTs shrink and grow are $l_{short} = v_s/f_{res}$ and $l_{grow} = v_g/f_{cat}$, respectively, during one dynamic instability cycle and, therefore, the sign of the expression ($v_s f_{cat} - v_g f_{res}$) is equivalent to the sign of ($l_{short} - l_{grow}$).

The following arguments provide a simple qualitative explanation for our experimental observations and model results. The spatial distribution of MT plus ends in the spindle is determined by l_{grow} and l_{short}. First, if $l_{grow} > l_{short}$, then, on average, MTs elongate more than shorten, and the mean length of MTs in the spindle, <*L*>, always increases; therefore, MTs rarely shorten all the way to the poles. Specifically, MT lengths are in the unbounded regime in this case, and <*L(t)*> increases by the length $J = (l_{grow} - l_{short})/(f + 1/f)$ per cycle, where $f = f_{cat}/f_{res}$ (Verde et al., 1992; note that because $[f + 1/f] \geq 2$ for all positive values of f, J is limited by $[l_{grow} - l_{short}]/2$), and MTs very rarely shorten to μm-range lengths. In this regime, as the mean MT length increases with time, in late preanaphase B (metaphase–anaphase A steady state), almost all MTs will have stable "stubs" near the poles, and these stable MT stubs only turn over by fluxing polewards: sliding and depolymerizing at the poles. Thus, MT turnover near the poles would be mostly due to poleward flux in late preanaphase B and therefore very slow and nearly linear. This indicates that the preanaphase B spindle must maintain a regime in which $l_{grow} < l_{short}$, and the MT lengths are distributed exponentially with mean length

$$< L >= \frac{l_{grow} l_{short}}{l_{short} - l_{grow}}.$$

In this regime, the first possibility is that both l_{grow} and l_{short} are small (in the μm or sub-μm range), whereas <*L*> is much greater than $l_{grow} \sim l_{short}$, and the MT plus ends make rapid and short back-and-forth excursions. Because of the shortness of these excursions, it would take a very long time for tubulin dimers near MT minus ends to turn over, so this regime also cannot account for the observed rapid FRAP rates near the poles. The second possibility in this regime is that both l_{grow} and l_{short} and <*L*> are very small (in the μm or sub-μm range, $l_{grow} << l_{short}$); however, in this case, the spindle integrity cannot be maintained as a result of a very small number of MTs that overlap at the spindle equator. Therefore, the only viable regime is if l_{grow} is of the same order and a little smaller than l_{short}, and both of these parameters are comparable with the half-size of the spindle. In this case, on average, MTs turn over almost entirely in a single cycle of shortening and growth, and consequently the recovery time does not depend on the size or position of the bleached region. The half-time of recovery after photobleaching is then simply the half-time of this cycle (which is $1/f_{res}$ or $1/f_{cat}$; they are of the same order).

To accommodate flux into the calculations at the beginning of the flux section, it suffices to adjust the apparent growth and shortening rates of the MTs, v_g^a and v_s^a (i.e., the velocities of growth and shortening in the lab frame of reference), as $v_g^a = v_g - v_{flux}$ and $v_s^a = v_s + v_{flux}$, where v_{flux} is the flux rate. Therefore, the net growth and shortening rates, v_g and v_s, we typically use in our simulations differ slightly from the values predicted through the mathematical estimates at the beginning of this section.

Model equations

Our quantitative model is based on three core equations that describe the dynamics of the spindle length S (1), and that of the antiparallel overlap L at the equator (2), and the force balance on the spindle poles (3) (Brust-Mascher et al., 2004).

$$\frac{dS}{dt} = 2(V_{sliding} - V_{depoly}) \quad (1),$$

$$\frac{dL}{dt} = 2(V_{netpoly} - V_{sliding}) \quad (2), \text{ and}$$

$$\frac{\mu}{2}\frac{dS}{dt} = NkLF_m\left(1 - \frac{V_{sliding}}{V_m}\right) \quad (3).$$

These equations were developed to describe the dynamics of the spindle poles from metaphase through anaphase B, based on the action of the bipolar motors that persistently slide ipMTs apart. During pre-anaphase B, the sliding is converted into flux by depolymerization of the MT minus ends at the poles, whereas in anaphase B, the suppression of depolymerization couples sliding to spindle elongation (Brust-Mascher et al., 2004). Implicit in these model equations are the following important assumptions. (1) The depolymerization rate of MT minus ends is limited by the sliding rate of ipMTs, and therefore the depolymerase KLP10A acts as an enzyme that does not generate noteworthy force on MTs or on the spindle poles. Therefore, in this model, a depolymerization rate that exceeds the sliding rate is prohibited, as depolymerization cannot drive the inward movement of the spindle poles because of lack of sufficient force generation to overcome drag (equations 1 and 3), and these equations cannot be considered to account for this situa-

tion (Goshima et al., 2005). However, it is possible that the depolymerase reels in "free" MTs that do not overlap antiparallel with other MTs at the maximal depolymerization rate, as the drag force on these free MTs is in the femtoNewton range and therefore negligible. (2) The outward force generated by the bipolar KLP61F motors is limited by the overlap length, *L*, and not by the number of motors available. Thus, these equations cannot be considered to account for the inhibition of the bipolar sliding motors, where the number of motors becomes the limiting factor for force generation (Goshima et al., 2005). Third, we assume that during metaphase the main motor on the ipMTs is the bipolar kinesin motor, and the minus end–directed kinesin, Ncd, does not have an effect in the metaphase steady state, as observed in the initial half of metaphase of the cycle 12 stage *Drosophila* embryonic spindles (Brust-Mascher and Scholey, 2002). In addition, we do not consider the effect of other possible force generators acting directly or indirectly on the spindle poles in this model (kinetochore tension, astral MT-based force, etc.).

Computational methods

A large system of equations, based on the three core equations in the Model equations section and described by Brust-Mascher et al. (2004) were used to describe the dynamics of the spindle poles, as well as the dynamics of the plus and minus ends of the spindle MTs from late prometaphase through anaphase B. The equations were solved numerically typically for 250 iterations, corresponding to 250 s in real time, where the initial 100 s mimic the prometaphase–metaphase transition period and the establishment of robust ipMT bundles, the following 100 s (from 100 to 200 s) mimic metaphase and anaphase A (preanaphase B steady- state), and the last 50 s (from 200 to 250 s) mimic anaphase B. The mean depolymerization rate of the minus ends of the spindle MTs are assumed to be the same from the initial time (t = 1 s) until the onset of anaphase B (t = 200 s), and the switch from metaphase–anaphase A steady state to anaphase B spindle elongation is achieved simply by turning off the depolymerization rate (setting v_{dep} = 0 μm/s) at t = 200 s in the code. An important part of the computer code used is the random number–generated stochastic variations of the model parameters. In the code, we assume that there are typically either 300–600 individual MTs emanating from each pole with their minus ends at the pole or 200 MT arrays, consisting of interdigitating short MTs, running from pole to pole, and each array consisting of two, three, or four short MTs (Fig. S3 B). For each MT in the spindle, we compute the positions of the plus ends that undergo dynamic instability and the minus ends that depolymerize until the onset of anaphase B, but not during anaphase B. At each computational step, the system of force balance and kinematic equations are solved based on the current positions of plus and minus ends and thus the current overlaps between the MTs (Brust-Mascher et al., 2004), by computing the force developed in each antiparallel/parallel overlap, the sliding velocity and the minus-end depolymerization rate for each MT, and the velocity of the spindle poles. Then,

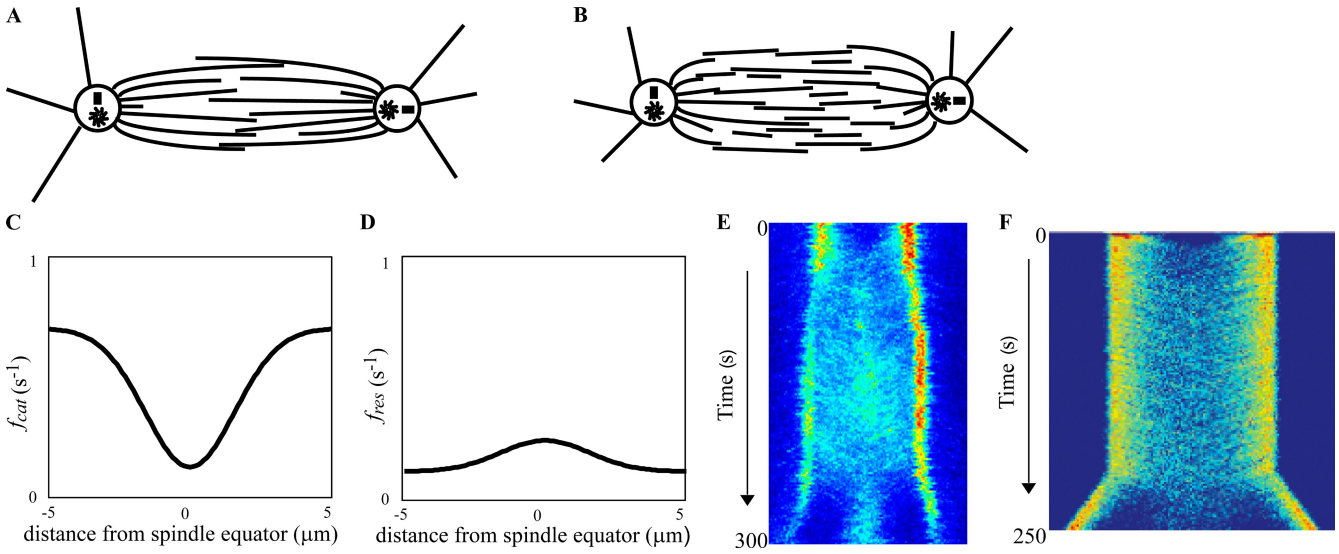

Figure S3. **MT minus-end distribution and MT catastrophe and rescue frequency profiles.** (A and B) Cartoons showing two possible organization of the MT minus and plus ends in a preanaphase B spindle. For simplicity, the chromosomes and the kMTs (assumed to be linked to the spindle poles at their minus ends and to the kinetochores at their plus ends) are not shown. (A) All minus ends of ipMTs are anchored at the spindle poles. (B) The ipMTs are composed of interdigitating short MTs and have both their plus and minus ends (nucleation sites) distributed along the spindle. (C) Catastrophe frequency profile along the spindle axis used for Fig. 6. (D) Typical rescue frequency profile along the spindle axis, used to test the possible effect of a rescue gradient on FRAP and EB1-GFP distribution at anaphase B transition, and the exact profile used for F, to account for the experimentally observed change in EB1 distribution at prometaphase–metaphase transition. (E) Kymograph of EB1-GFP from prometaphase until telophase from experiment. (F) Kymograph of growing MT plus ends (mimicking the experimental EB1-GFP kymograph). High to low concentration positions of growing plus ends within the spindle are shown over time (vertical axis) in bright to dark colors, respectively, from early prometaphase through anaphase B (total of 250 s). In the simulation, a gradient of rescue frequency (as shown in Fig. S3 D with maximal value f_{res} = 0.15 s^{-1} at the equator and minimum f_{res} = 0.075 s^{-1}) was used from the initial time step until the end, and a gradient of catastrophe (as shown in Fig. S3 C with minimum value f_{cat} = 0.2 s^{-1} at the equator and maximum rate f_{cat} = 0.6 s^{-1}), which was introduced at the onset of anaphase B (time = 200 s). The growth and shortening rates are v_g = v_s = 0.34 μm/s, and all other parameters are as in Table S1.

the plus ends are allowed to grow or shorten depending on the computed rescue/catastrophe frequencies of the MT plus end, and finally the new positions of all the MT ends and that of the spindle poles are updated to be used in the next time step.

We used random number generators (MATLAB built-in rand and randn functions) for the initial configurations of MTs and the fluctuations in MTs' polymerization and depolymerization rates and to decide whether a rescue or catastrophe event occurs at the plus ends of each MT at each time step. Explicit forward Euler method was used to solve the equations of motion for the MTs and poles numerically on a desktop computer. The codes were implemented in MATLAB. One computational step, Δt, corresponds to 1 s. The parameter values and model variables are summarized in Table S1. Only orders of magnitude of most model parameters are available from the literature, so we chose the actual values in the simulations to obtain the best possible fit to the data.

FRAP simulations

To simulate FRAP experiments (Brust-Mascher et al., 2004), we first calculate the total length of MTs within the predetermined bleach region, e.g., the region (−5,0) for the half-spindle, or (−5,−3) for a 2-μm wide region near the pole, or (−1,1) for a region at the spindle equator. These values are stored in an array, representing the total fluorescence intensity in the region of interest, assuming that the fluorescence intensity in a given region reflects the total length of labeled tubulin in assembled (MT) form. At the time of the bleach, the total length of MTs in the bleach region and the locations of the ends of the bleached MT portions are stored in separate arrays, and the total fluorescence intensity is set to zero at the time of the bleach, portraying a full and complete irradiation of the MTs in the bleach region. The fates of the irradiated and fluorescent labeled portions of the MT lattices are computed in the same way, through dynamic instability and sliding and flux, when it applies. During the time steps after the bleach time, the total length of the nascent fluorescent portions of MTs in the bleach zone is calculated and stored in the array of total fluorescence intensity; these values are plotted over time and fit by a single exponential curve to calculate the $t_{1/2}$. In Videos 6 and 7, MTs with their minus ends near or anchored at the left spindle pole are always shown in green, those with their minus ends near or anchored at the right pole are shown in yellow, and the bleached portions of both populations of MTs are shown in red. In Video 5, the spindle MTs is separated in nine different groups (e.g., first group including the MTs numbered from 1 to 66, the second group of MTs numbered from 67 to 133, etc., for a spindle with a total of 600 MTs emanating from each pole) and the fluorescence intensity of MTs in each group, at each time step, is plotted in a thin elliptical line, in vertical bins of 0.1-μm width, mimicking the nine ipMT bundles in the spindle and simulating the "crowding" effect of MTs near the poles. Before plotting, a Gaussian centered at 0 and variance <10% of the maximum (randn function in MATLAB) was added to the fluorescence values to simulate the noise in experimental data.

Searching the MT dynamics parameter space for rapid FRAP rates

A subspace of the four dimensional parameter space (v_g, v_s, f_{cat}, and f_{res}) comprising the biologically relevant parameters of MT dynamics was systematically explored to determine which combinations of these parameters can account for the observed rapid FRAP rates in the spindle. To this end, the values for v_g and v_s were varied between 0.1 and 0.34 μm/s in steps of 0.06 μm/s, and the values for f_{cat} and f_{res} were varied from 0.05 and 0.25 s^{-1} in steps of 0.05 s^{-1}. For each one of the 256 combination of these MT dynamic rates, the positions of the ends of all MTs and the spindle poles (the sliding rate of each MT, the depolymerization rate of all minus ends, and the growth/shortening of all the plus ends of MTs) were computed (as described in the Computational methods section) for 250 s (from late prometaphase to anaphase B) and stored. The combinations of parameters for which the antiparallel overlap was

Table S1. **Model variables and parameters**

Symbol	Meaning	Value	Reference
Model variables			
S	Distance between spindle poles	Variable	
L	ipMT overlap distance	Variable	
$V_{sliding}$	Rate of speckles sliding away from the equator	Variable	
Model parameters with little effect on the rate of early anaphase B			
F_m	Maximal motor force	1 pN	Valentine et al., 2006
N	Number of overlapping pairs of ipMTs	200–600	Sharp et al., 1999; Brust-Mascher et al., 2004
k	Number of motors per unit length	10–20 μm^{-1}	Sharp et al., 1999
μ	Effective spindle viscous drag coefficient	1,000 pN•s/μm	Marshall et al., 2001
$V_{netpoly}$	Net plus-end polymerization rate	0.01–0.1 μm/s	Rusan et al., 2002
v_g	MT plus-end growth rate	0.1–0.34 μm/s	Rogers et al., 2002; Rusan et al., 2002
v_s	MT plus-end shortening rate	0.1–0.34 μm/s	Rogers et al., 2002; Rusan et al., 2002
f_{res}	MT plus-end rescue frequency	0.01–0.5 s^{-1}	Rogers et al., 2002; Rusan et al., 2002
f_{cat}	MT plus-end catastrophe frequency	0.01–0.5 s^{-1}	Rogers et al., 2002; Rusan et al., 2002
Model parameters that affect the rate of anaphase B			
V_m	Free sliding rate of KLP61F	0.05 μm/s	Valentine et al., 2006
V_{depoly}	Minus-end depolymerization rate	Variable (0-0.05 μm/s)	Brust-Mascher and Scholey, 2002; Brust-Mascher et al., 2004

not sustained during metaphase (because of very low rate of net plus-end polymerization) were marked as bad combinations and were not considered further. For the remaining combinations of the MT dynamic parameters, using the corresponding and previously computed spindle MT dynamics, the bleaching of the entire half-spindle was simulated, the fluorescence recovery curve was plotted, fitted by a single exponential curve, based on which the FRAP $t_{1/2}$ was calculated and stored.

Generation of the EB1-GFP kymograph

In the simulations, the state of each MT plus end at each time step is stored in an array. To mimic the observed EB1-GFP distribution, which marks the growing plus ends of MTs in the spindle, the histogram of the plus ends currently in the growth state are plotted in the form of a kymograph.

Spindle architecture

In our simulations, we consider two different spindle architectures (Fig. S3, A and B). First, we consider a spindle in which MTs have their minus ends anchored at the spindle poles and their plus ends extending toward the spindle equator, where some MTs overlap antiparallel with MTs extending from the opposite pole (Fig. S3 A). Second, we consider a spindle composed of a mixed population of ipMTs, some with their minus ends anchored at the spindle poles and extending toward and overlapping antiparallel at the spindle equator, and other ipMTs that are composed of short, interdigitating MTs with both minus and plus ends of MTs distributed along the spindle (Fig. S3 B). It is possible to recover the observed rapid and uniform FRAP rates in both spindle types; however, the range of parameter values that can account for the observed rapid FRAP rates is wider for the second spindle architecture (Fig. S3 B), where the minus ends of short MTs are distributed along the spindle. Nevertheless, in this case, along with the high flux rates characteristic of the *Drosophila* spindles, if we assume that (1) the nucleation sites along the spindle emerge continuously at random positions along the spindle (i.e., when an MT disassembles fully during a dynamic instability cycle, if we assume that a new MT in the spindle nucleates spontaneously at a random position along the spindle), most spindles with MT dynamic rates that can potentially give rise to the rapid FRAP kinetics cannot maintain a sufficient overlap during metaphase (spindle integrity is compromised), and thus these spindles are not viable (unpublished data) or, alternatively (2) that the nucleation sites are permanent and thus flux polewards (i.e., when an MT disassembles entirely during a dynamic instability cycle, if we assume that a new MT spontaneously nucleates at the same site), then all (or almost all) nucleation sites/minus ends are transported to the opposing spindle poles during preanaphase B, altering the spindle architecture severely (unpublished data), reverting it back to the one given in Fig. S3 A. To summarize, a spindle composed of interdigitating short MTs, with minus ends along the spindle, and new MTs emerging at random positions along the spindle, cannot maintain sufficient antiparallel overlap if the MT dynamics and flux rates are high (MT life time < 20–30 s; flux rate ∼0.05 μm/s), and if the MTs nucleation sites are permanent and thus flux polewards, the spindle reverts back to the architecture given in Fig. S3 A during preanaphase B (in ∼50–75s), where most MT minus ends at the poles. Therefore, this possibility was not considered further.

Flux contributes minimally to the MT turnover observed by FRAP, but it may influence spindle integrity by restricting the length of spindle MTs

In the fly embryo, the flux rates of MTs during the metaphase and anaphase A are rapid compared with other organisms (Brust-Mascher and Scholey, 2002; Maddox et al., 2002; Rogers et al., 2004), so we wanted to determine if this high flux rate contributes to the observed fast FRAP rates. To assess this, we simulated a preanaphase B half-spindle FRAP using MT dynamic instability parameters that give rise to rapid FRAP rates ($t_{1/2}$ = 5–8 s, as shown in Fig. 5, A and B) both with and without flux. To simulate hypothetical *Drosophila* embryo spindles that display no flux, we retained the same f_{cat} and f_{res} values as before, but we modified the growth and shortening such that, $v_g^{no\text{-}flux} = v_g - v_{flux}$ and $v_s^{\text{no-flux}} = v_s + v_{flux}$ in order to simulate the corresponding dynamic rates in both conditions (note that in the presence of flux, the growth and shortening velocities of plus ends in the lab frame of reference [i.e., with respect to an observer who is placed, for example, on the spindle pole] are $v_g - v_{flux}$, and $v_s + v_{flux}$; see Mathematical estimates of MT lengths and turnover time). We find that, in this rapid MT turnover regime, flux does not contribute to the rapid FRAP rate when we simulate the bleaching of the half-spindle or to the recovery of smaller bleach regions. Interestingly, however, if we use the same values for v_g and v_s in our no-flux simulations, i.e., $v_g^{no\text{-}flux} = v_g$ and $v_s^{\text{no-flux}} = v_s$, the pole-to-pole MTs become "overgrown," with most MT plus ends near the opposite spindle pole by late preanaphase B, thereby disrupting spindle integrity. This suggests that one important function of the high poleward flux rates found in the *Drosophila* embryo may be to ensure coherent spindle architecture in the face of rapid MT dynamics.

Number and dynamics of kMTs in the metaphase spindle

Previous studies have shown that during metaphase, kMTs display slower dynamics than non-kMTs (Gorbsky and Borisy, 1989; DeLuca et al., 2006). Our experimental FRAP data of regions near the poles and the equator of the metaphase spindle are indistinguishable, and both display an excellent fit to a single exponential recovery profile, suggesting that (1) both kMTs and non-kMTs undergo similar dynamics, (2) the kMTs are more stable than the non-kMTs, but the number of kMTs is much smaller than that of non-kMTs, or (3) the kMTs are more stable than the non-kMTs and the number of kMTs is comparable to that of non-kMTs at the early stages of metaphase, but there is an increase in the number of non-kMTs that conceals the lack of recovery of the stable kMTs in the metaphase FRAP data.

Table S2. **Number and dynamics of kMTs in the metaphase spindle from modeling**

Percentage of kMTs	Percentage of recovery near the poles during metaphase	Recovery half-time
no. of kMT /no. of non-kMTs		*s*
50 (56/60)	45–50	5
40 (56/80)	70	8
20 (56/200)	80–85	8.5
10 (56/500)	90	9
7 (56/750)	95–100	10

EM data on related organisms to the *Drosophila* embryo, namely, the fly spermatocyte (Maiato and Sunkel, 2004) and the *Drosophila* S2 cell line (Vandenbeldt et al., 2006; Maiato et al., 2006) and our earlier modeling work (Civelekoglu-Scholey et al., 2006) suggest that there are ∼5–10 kMTs per kinetochore in the spindle. Therefore, in our simulations, we considered approximately seven kMTs per kinetochore and examined how the FRAP half-time increases with an increasing ratio of kMTs (that are highly dynamic but rescue rapidly at the kinetochore–MT interface because of sister kinetochore tension and are therefore stabilized along their length) to non-kMTs (that rescue/catastrophe and grow and shrink at a constant rate throughout the spindle), using the range of MT dynamicity parameters that can account for the observed FRAP rates. We found that as the ratio of the kMT to spindle MTs (kMT + non-kMT) varies from 7% (56 kMTs and 750 non-kMTs) to 50% (56 kMTs and 60 non-kMTs), the half-time of FRAP increases only from 5 to 10 s (Table S2), and the fluorescence recovery curve, in the time frame of interest (50 s) is fit very well by a single exponential, remaining comparable to experimentally observed rates. If the proportion of kMTs in the spindle is >50%, this rate increases rapidly toward 20–30 s, the recovery curve becomes linear rather than exponential, and the extent of FRAP near the poles decreases well below 40–50%, incompatible with our experimental observations. In the simulations, the extent of FRAP near the poles fits our experimental observation best when kMTs comprise 10% or less of the spindle MTs throughout metaphase, favoring the second possibility considered in the beginning of this section.

EB1-GFP redistribution at anaphase B onset

We consider two possibilities that can potentially account for the reduced extent of FRAP near the poles at anaphase B: (1) the possibility of a spatial gradient of rescue or catastrophe, which sets in the spindle at anaphase B onset, and (2) a change in the spatial MT minus-end distribution at anaphase B onset.

In the first case, we investigated two possibilities: (1) a gradient of catastrophe, with high catastrophe rate near the poles and low rate near the equator (Fig. S3 C) or (2) a gradient of rescue, with low rescue rate near the poles and high rate near the equator (Fig. S3 D). For the range of gradient strengths, we tested in our simulations (from no gradient, maximum frequency = minimum frequency, to a very strong gradient, maximum frequency = 10× minimum frequency), the onset of a rescue frequency gradient at metaphase–anaphase B transition altered the dynamics of spindle MTs and accounted well for the EB1-GFP redistribution. However, (1) FRAP simulations near the poles gave very slow recoveries, where the recovery is incomplete but very fast and (2) the FRAP simulations at the equator were incomplete, i.e., there was a substantial loss in long MTs overlapping at the spindle equator, inconsistent with our experimental results. On the other hand, the onset of a catastrophe frequency gradient at the anaphase B transition altered the dynamics of spindle MTs in a way that reproduced both the EB1-GFP redistribution at anaphase B onset and our FRAP results in different regions of the anaphase B spindle. The best fit to our experimental observations (Fig. 6) was obtained with a gradient that was three times higher near the poles than at the equator (Fig. S3 C).

In the second case (a change in the spatial MT minus-end distribution at anaphase B onset), we assume that the MT minus ends' anchorage to the spindle poles requires the active form of the depolymerase KLP10A and that KLP10A is inactivated at anaphase B onset (Rogers et al., 2004). In this situation, after the inactivation of KLP10A at the poles at anaphase B onset, only antiparallel overlapping ipMTs are slid apart and their minus ends maintain contact with the spindle poles while they push the poles apart, and all other free MTs, or MTs that become free by loosing their antiparallel overlap are released from the poles, stop sliding and undergo diffusion. The simulation results show that this mechanism also accounts well for the EB1-GFP redistribution in the spindle but gives rise to a very slow FRAP recovery near the pole, inconsistent with our experimental results (recovery near the pole is fast but incomplete).

The change in EB1-GFP distribution from prometaphase to metaphase can be accounted for by a gradient of rescue frequency in the spindle

Because we observe a change in the EB1-GFP distribution at the prometaphase–metaphase transition (Fig. S3 E), we investigated this phenomenon theoretically as well. We looked for a change in MT dynamics that would lead from an uneven distribution of growing MT plus ends, where most growing MT plus ends are concentrated closer to the poles (short MTs), to a uniform distribution across the spindle. In particular, we explored the following two possibilities: (1) the establishment of a catastrophe frequency gradient characterized by baseline catastrophe frequency near poles and decreased catastrophe frequency at spindle equator, whereas the rescue frequency remained constant in space, and (2) the establishment of a rescue frequency gradient characterized by baseline res-

cue frequency near poles, and increased rescue frequency at spindle equator, whereas the catastrophe frequency remained constant. Although the first possibility accounts for the change in the growing MT plus ends' distribution well at the prometaphase–metaphase transition, it accounts poorly for the observed uniform FRAP in the spindle during metaphase. However, the establishment of a rescue frequency gradient late in prometaphase, with baseline rescue frequency near poles and higher (twofold) frequency near the spindle equator (Fig. S3 D), and a gradient of catastrophe frequency at anaphase B onset (Fig, S3 C), accounts very well for both the changes in the growing plus-end distribution at prometaphase–metaphase transition, and that at the anaphase B transition (Fig. S3 F), and all our FRAP observations through anaphase B (unpublished data). The establishment of a weak gradient in the rescue frequency in the spindle would give rise to an overall increase in the rescue frequency of MTs at the prometaphase–metaphase transition, which is consistent with earlier observations in mitotic cells.

Materials and methods

Microinjection of antibody and recombinant protein into embryos

Affinity purification and microinjection of anti-KLP3A antibody and RanT24N protein 0–2-h embryos was performed as described previously (Kwon et al., 2004; Silverman-Gavrila and Wilde, 2006).

References

Brust-Mascher, I., and J.M. Scholey. 2002. Microtubule flux and sliding in mitotic spindles of *Drosophila* embryos. *Mol. Biol. Cell*. 13:3967–3975.

Brust-Mascher, I., G. Civelekoglu-Scholey, M. Kwon, A. Mogilner, and J.M. Scholey. 2004. Model for anaphase B: role of three mitotic motors in a switch from poleward flux to spindle elongation. *Proc. Natl. Acad. Sci. USA*. 101:15938–15943.

Civelekoglu-Scholey, G., D.J. Sharp, A. Mogilner, and J.M. Scholey. 2006. Model of chromosome motility in *Drosophila* embryos: adaptation of a general mechanism for rapid mitosis. *Biophys J*. 90:3966–3982.

DeLuca, J.G., W.E. Gall, C. Ciferri, D. Cimini, A. Musacchio, and E.D. Salmon. 2006. Kinetochore microtubule dynamics and attachment stability are regulated by Hec1. *Cell*. 127:969–982.

Gorbsky, G.J., and G.G. Borisy. 1989. Microtubules of the kinetochore fiber turn over in metaphase but not in anaphase. *J. Cell Biol*. 109:653–662.

Goshima, G., R. Wollman, N. Stuurman, J.M. Scholey, and R.D. Vale. 2005. Length control of the metaphase spindle. *Curr. Biol*. 15:1979–1988.

Kwon, M., S. Morales-Mulia, I. Brust-Mascher, G.C. Rogers, D.J. Sharp, and J.M. Scholey. 2004. The chromokinesin, KLP3A, dives mitotic spindle pole separation during prometaphase and anaphase and facilitates chromatid motility. *Mol. Biol. Cell*. 15:219–233.

Maddox, P., A. Desai, K. Oegema, T.J. Mitchison, and E.D. Salmon. 2002. Poleward microtubule flux is a major component of spindle dynamics and anaphase A in mitotic *Drosophila* embryos. *Curr. Biol*. 12:1670–1674.

Maiato, H., and C.E. Sunkel. 2004. Kinetochore-microtubule interactions during cell division. *Chromosome Res*. 12:585–597.

Maiato, H., P.J. Hergert, S. Moutinho-Pereira, Y. Dong, K.J. Vandenbeldt, C.L. Rieder, and B.F. McEwan. 2006. The ultrastructure of the kinetochore and kinetochore fiber in *Drosophila* somatic cells. *Chromosoma*. 115:469–480.

Marshall, W.F., J.F. Marko, D.A. Agard, and J.W. Sedat. 2001. Chromosome elasticity and mitotic polar ejection force measured in living *Drosophila* embryos by four-dimensional microscopy-based motion analysis. *Curr. Biol*. 11:569–578.

Rogers, G.C., S.L. Rogers, T.A. Schwimmer, S.C. Ems-McClung, C.E. Walczak, R.D. Vale, J.M. Scholey, and D.J. Sharp. 2004. Two mitotic kinesins cooperate to drive sister chromatid separation during anaphase. *Nature*. 427:364–370.

Rogers, S.L., G.C. Rogers, D.J. Sharp, and R.D. Vale. 2002. *Drosophila* EB1 is important for proper assembly, dynamics, and positioning of the mitotic spindle. *J. Cell Biol*. 158:873–884.

Rusan, N.M., U.S. Tulu, C. Fagerstrom, and P. Wadsworth. 2002. Reorganization of the microtubule array in prophase/prometaphase requires cytoplasmic dynein-dependent microtubule transport. *J. Cell Biol*. 158:997–1003.

Sharp, D.J., K.L. McDonald, H.M. Brown, H.J. Matthies, C. Walczak, R.D. Vale, T.J. Mitchison, and J.M. Scholey. 1999. The bipolar kinesin, KLP61F, cross-links microtubules within interpolar microtubule bundles of *Drosophila* embryonic mitotic spindles. *J. Cell Biol*. 144:125–138.

Silverman-Gavrila, R.V., and A. Wilde. 2006. Ran is required before metaphase for spindle assembly and chromosome alignment and after metaphase for chromosome segregation and spindle midbody organization. *Mol. Biol. Cell*. 17:2069–2080.

Valentine, M.T., P.M. Fordyce, T.C. Krzysiak, S.P. Gilbert, and S.M. Block. 2006. Individual dimers of the mitotic kinesin motor Eg5 step processively and support substantial loads in vitro. *Nat. Cell Biol*. 8:470–476. Vandenbeldt, K.J., R.M. Barnard, P.J. Hergert, X. Meng, H. Maiato, and B.F. McEwen. 2006. Kinetochores use a novel mechanism for coordinating the dynamics of individual microtubules. *Curr. Biol*. 16:1217–1223.

Verde, F., M. Dogterom, E. Stelzer, E. Karsenti, and S. Leibler. 1992. Control of microtubule dynamics and length by cyclin A- and cyclin B-dependent kinases in *Xenopus* egg extracts. *J. Cell Biol*. 118:1097–1108.